Collective Collapse of a Bose-Einstein Condensate with Attractive Interactions

C. A. Sackett, J. M. Gerton, M. Welling, and R. G. Hulet[1]

Physics Department, MS 61
Rice University
Houston, TX 77251

Abstract. Bose-Einstein condensation (BEC) of atoms with attractive interactions is profoundly different from BEC of atoms with repulsive interactions, in several respects. We describe experiments with Bose condensates of ^{7}Li atoms, which are weakly attracting at ultralow temperature. We measure the distribution of condensate occupation numbers occurring in the gas, which shows that the number is limited and demonstrates the dynamics of condensate growth and collapse.

INTRODUCTION

The recent attainment of Bose-Einstein condensation (BEC) of dilute atomic gases [1–3] has enabled new investigations of weakly interacting many-body systems. ^{7}Li is unique among these gases in that the interactions are effectively attractive. These attractive interactions profoundly effect the nature of BEC. In fact, it was long believed that attractive interactions precluded the attainment of BEC in the gas phase [4,5]. It is now known that BEC *can* exist in a confined gas, provided the condensate number remains small [6]. These condensates are predicted to exhibit fascinating dynamical behavior, including soliton formation [7] and macroscopic quantum tunneling [8–11]. This paper reviews our work on BEC of ^{7}Li, including the measurement of limited condensate number, and the dynamics of condensate growth and collapse.

INTERACTIONS IN DILUTE GASES

One of the primary interests in dilute Bose-Einstein condensates is that the interactions are weak, facilitating comparison between theory and experiment. When

[1)] This work is supported by the National Science Foundation, the Office of Naval Research, NASA, and the Welch Foundation.

the de Broglie wavelength Λ is much longer than the characteristic two-body interaction length, the effect of the interaction can be represented by a single parameter, the s-wave scattering length a [12]. The magnitude of a indicates the strength of the interaction, while the sign determines whether the interactions are effectively attractive ($a < 0$) or repulsive ($a > 0$). In the experiments, the density n is small enough that $n|a|^3 \ll 1$, so only binary interactions need be considered.

Photoassociative Spectroscopy

Although the interaction potentials for hydrogen and the alkali-metal atoms through francium are all qualitatively the same, in that they all have a repulsive inner-wall, a minimum that supports vibrational bound states (except for the triplet potential of hydrogen), and a long-range van der Waals tail, their respective scattering lengths differ enormously in magnitude and in sign. This variation arises because of differences in the proximity of the least-bound vibrational state to the dissociation limit. As with the familiar attractive square-well potential, a barely bound or barely unbound state leads to collisional resonances that produce very large magnitude scattering lengths. Therefore, small changes in the interaction potential may result in a large change in the magnitude, or even change the sign of a. In the past few years, photoassociative spectroscopy of ultracold atoms has proven to be the most precise method for determining scattering lengths [13]. In one-photon photoassociation, a laser beam is passed through a gas of ultracold atoms confined to a trap. As the laser frequency is tuned to a free-bound resonance, diatomic molecules are formed resulting in a detectable decrease in the number of trapped atoms. The intensity of the trap-loss signal is sensitive to the ground-state wavefunction, providing useful information for determining the ground-state interaction potential. The value of the scattering length is found by numerically solving the Schrödinger equation using this potential. This method has been used to find the scattering lengths for Li, Na, K, and Rb [13].

A more precise method for finding scattering lengths is to probe the ground state molecular levels directly. In particular, the scattering length is extremely sensitive to the binding energy of the least-bound molecular state. We have used two-photon photoassociation to directly measure this binding energy for both stable isotopes of lithium, the bosonic isotope ^{7}Li [14] and the fermionic isotope ^{6}Li [15]. In this method, a laser is tuned to the free-bound transition as in one-photon photoassociation, while the frequency of a second laser is tuned to resonance between the bound excited state and a bound ground state. The frequency difference between the two lasers gives the binding energy directly. This technique has resulted in the most precisely known atomic potentials. Table 1 gives the triplet and singlet scattering lengths for both isotopes individually, as well as for mixed isotope interactions. A summary of our scattering length measurements in lithium is given in Ref. [15]. Two-photon spectroscopy of the ground-state has also been used recently to find the scattering lengths of rubidium [16].

TABLE 1. Singlet and triplet scattering lengths in units of a_o, for isotopically pure and mixed gases of lithium isotopes [15]. The singlet scattering lengths were determined from one-photon photoassociative spectra, while the triplets were determined using the two-photon technique. The mixed case scattering lengths were calculated from knowledge of the $^6Li_2$ and $^7Li_2$ potentials

	^{6}Li	^{7}Li	^{6}Li/^{7}Li
a_T	-2160 ± 250	-27.6 ± 0.5	40.9 ± 0.2
a_S	45.5 ± 2.5	33 ± 2	-20 ± 10

Mean-Field Theory

The effects of interactions on the condensate have been studied using mean-field theory and neglecting inelastic collisions [17]. In this approximation, the interaction part of the Hamiltonian is replaced by its mean value, resulting in an interaction energy of $U = 4\pi\hbar^2 an/m$, where n is the density and m is the atomic mass [12]. For a gas at zero temperature, the net result of the interactions and the confining potential can be found by solving the non-linear Schrödinger equation for the wave function of the condensate, $\psi(r)$ [18]:

$$\left(-\frac{\hbar^2}{2m}\nabla^2 + V(r) + U(r) - \mu\right)\psi = 0. \tag{1}$$

Here μ is the chemical potential, and $V(r)$ is the confining potential provided by the trap. In a spherically symmetric harmonic trap with oscillation frequency ω, $V(r) = m\omega^2 r^2/2$. The interaction energy $U(r)$ is determined by taking $n(r) = |\psi(r)|^2$.

Implications of $a < 0$

Limited Condensate Number

For a dilute gas with $a > 0$, corresponding to repulsive interactions, it was shown long ago that the condensate will be stable and that its properties, such as its critical temperature T_c or its elementary excitation spectra, can be found from a perturbation expansion in the small parameter na^3 [12]. However, for $a < 0$ the situation is drastically different. Since U decreases with increasing n, an untrapped (homogeneous) gas is mechanically unstable to collapse. Therefore, it was believed that BEC was not possible in the gas phase. In a system with finite volume, however, the zero-point kinetic energy of the atoms provides a stabilizing influence. A numerical solution to Eq. (1) is found to exist only when N_0 is smaller than a limiting value N_m [19]. Physically, this limit can be understood as requiring that the interaction energy U be small compared to the trap level spacing $\hbar\omega$, so that the

interactions act as a small perturbation to the ideal-gas solution. This condition implies that N_m is of the order $l_0/|a|$, where $l_0 = (\hbar/m\omega)^{1/2}$ is the length scale of the single-particle trap ground state [20]. It is at first surprising that N_m increases proportional to l_0, since it is known that BEC cannot occur in a homogeneous gas. However, the density of the condensate, N_0/l_0^3, tends to zero as $l_0 \to \infty$. This tradeoff between N_m and n is an important consideration when designing an experiment.

For condensate occupation numbers below N_m, ψ is determined using Eq. (1). It is found that for $N_0 \ll N_m$, ψ is closely approximated by the single-particle ground state, and as N_0 increases, the interaction energy causes the spatial extent of ψ to decrease. Note that even when a solution to Eq. (1) exists it represents only a metastable state of the trapped atoms [8–10,21], since the equilibrium state of lithium at low temperatures is a crystalline metal solid. Also, for temperatures $T > 0$, Eq. (1) must be modified to take into account the presence of thermally excited atoms, and N_m is slightly lower [21,22].

A variational method has been used to study the decay of condensates with attractive interactions [23,9,10], which we discuss here following the development of Stoof [10]. The ground-state solution to Eq. (1), ψ_0, satisfies an extremal condition

$$\langle\psi_0|H|\psi_0\rangle \leq \langle\psi|H|\psi\rangle \tag{2}$$

for any other function ψ. The energy operator H is given by

$$H = -\frac{\hbar^2}{2m}\nabla^2 + V(r) + \frac{U(r)}{2}, \tag{3}$$

where the factor of $1/2$ in the interaction term arises from the dependence of U on ψ. Because the solution to Eq. (1) for the ideal gas is a Gaussian function, it is reasonable to minimize $\langle H\rangle$ using the set of Gaussian trial wavefunctions

$$\psi(r;l) = \left(\frac{N_0}{\pi^{3/2}l^3}\right)^{1/2} \exp\left(-\frac{r^2}{2l^2}\right). \tag{4}$$

Evaluating $\langle H\rangle \equiv H(l)$ yields

$$H(l) = N_0\frac{\hbar^2}{m}\left(\frac{3}{4l^2} + \frac{3l^2}{4l_0^4} - \frac{|a|}{\sqrt{2\pi}}\frac{N_0}{l^3}\right). \tag{5}$$

This function is plotted for three values of N_0, in Fig. 1. It is observed that for sufficiently small N_0, a local minimum exists near $l = l_0$, indicating that a metastable condensate is possible. For larger N_0, however, the minimum vanishes, and the system will be unstable. The condition for stability is $N_0 \leq 0.68\, l_0/|a|$, which is in reasonable agreement with the exact value obtained by numerical integration of Eq. (1), $N_m = 0.58\, l_0/|a|$ [19]. At very small l, the density is sufficiently high that Eq. (1) is no longer valid, so the divergence of H as $l \to 0$ is of no concern, since it means only that the true ground state of the system is not a dilute gas.

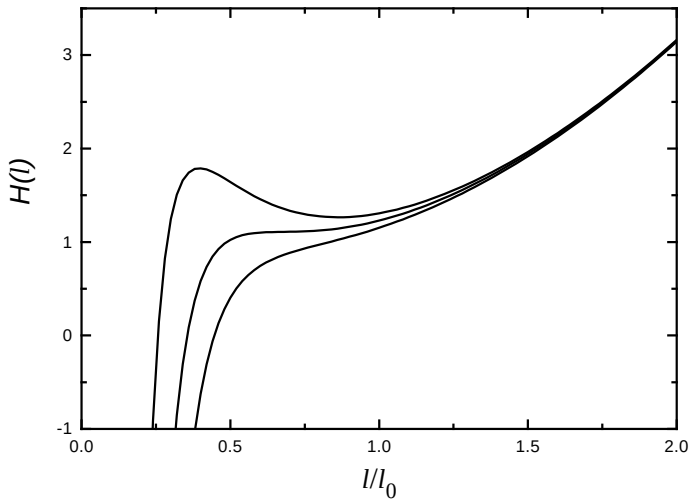

FIGURE 1. The condensate energy H, plotted in units of $N_0\hbar^2/ml_0^2$. The upper curve corresponds to $N_0 = 0.48\, l_0/|a|$, the middle curve to $N_0 = 0.68\, l_0/|a|$, and the lower curve to $N_0 = 0.87\, l_0/|a|$. It is evident that a local minimum in H exists near $l = l_0$ if N_0 is sufficiently low, indicating that a metastable condensate can exist.

We have extended the variational calculation to the case of a cylindrically symmetric trap [20]. We find that N_m is determined by the direction of tightest confinement, so that the stability condition can be expressed as

$$N_m \approx \frac{l_{min}}{|a|}, \tag{6}$$

where l_{min} is the lesser of $l_{0\rho}$ and l_{0z}. This result is in agreement with those of Ueda *et al.* [11]. Therefore, we find that a spherically symmetric trap is optimal for most purposes, as it provides the highest density for a given N_m.

Condensate Collapse

Although a condensate can exist in a trapped gas, it is predicted to be metastable and to decay by quantum or thermal fluctuations [8–11]. The condensate has only one unstable collective mode, which in the case of an isotropic trap corresponds to the breathing mode [7,23]. The condensate therefore collapses as a whole, either by thermal excitation over, or by macroscopic quantum mechanical tunneling through the energy barrier in configuration space, shown in Fig. 1.

The rates of decay for both quantum tunneling and thermal excitation can be calculated within the formalism of the variational calculation [10] and are shown in Fig. 2. For large numbers of condensate atoms, these collective decay mechanisms are much faster than the decay caused by inelastic two and three-body collisions, since the energy barrier out of the metastable minimum vanishes as N_0 approaches N_m.

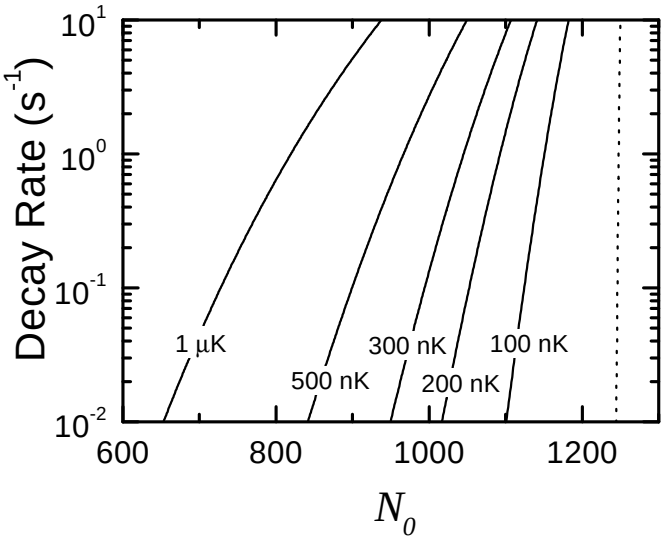

FIGURE 2. Decay rate of the condensate as a function of the number of condensate particles at several temperatures. The dotted line shows the macroscopic quantum tunneling rate.

Condensate Growth and Collapse During Evaporation

Experimentally, the condensate is formed by evaporatively cooling the gas. As the gas is cooled below the critical temperature for BEC, N_0 grows until N_m is reached. The condensate then collapses spontaneously if $N_0 \geq N_m$, or the collapse can be initiated by thermal fluctuations or quantum tunneling for $N_0 \simeq N_m$ [8–11,24]. During the collapse, the condensate shrinks on the time scale of the trap oscillation period. As the density rises, the rates for inelastic collisions such as dipolar decay and three-body molecular recombination increase. These processes release sufficient energy to immediately eject the colliding atoms from the trap, thus reducing N_0. The ejected atoms are very unlikely to further interact with the gas before leaving the trap, since the density of noncondensed atoms is low. As the collapse proceeds, the collision rate grows quickly enough that the density remains small compared to a^{-3} and the condensate remains a dilute gas [24,25]. However, the theories are not yet conclusive as to what fraction of the condensate atoms participates in the collapse, and of those participating, what fraction is eventually ejected.

Both the collapse and the initial cooling process displace the gas from thermal equilibrium. As long as N_0 is smaller than its equilibrium value, as determined by the total number and average energy of the trapped atoms, the condensate will continue to fill until another collapse occurs. This results in a cycle of condensate growth and collapse, which repeats until the gas comes to equilibrium with some $N_0 < N_m$. We have modeled the kinetics of the equilibration process by numerical solution of the quantum Boltzmann equation, as described in Ref. [24]. Fig. 3 shows a typical trajectory of N_0 in time, for our experimental conditions. In this

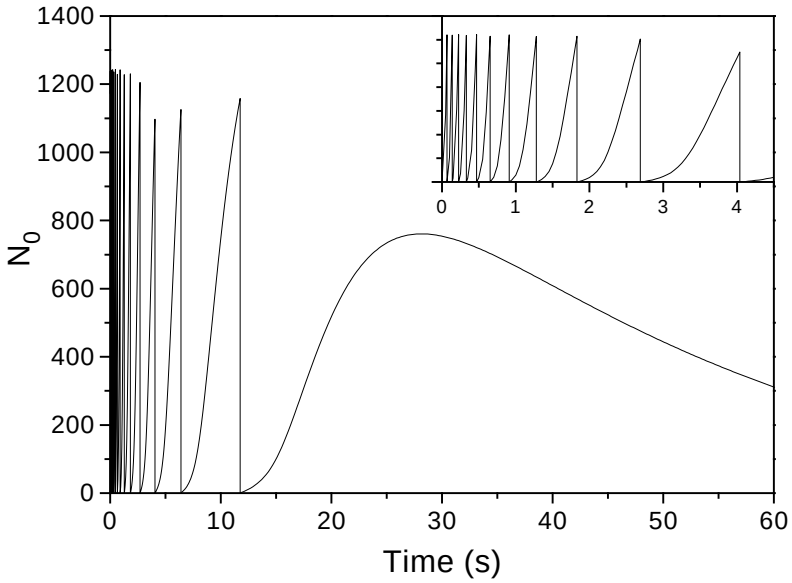

FIGURE 3. Numerical solution of the quantum Boltzmann equation, showing evolution of condensate occupation number. A trapped, degenerate ^{7}Li gas is cooled at $t = 0$ to a temperature of about 100 nK and a total number of 4×10^4 atoms. The gas then freely evolves in time. The inset shows an expanded view of the early time behavior on the same vertical scale.

calculation we assumed that N_0 is reduced to zero when a collapse occurs, on the basis of the model proposed in Ref. [24].

Relation to Other Collapse Phenomena

The non-linear Schrödinger equation (Eq. (1)) has been used to describe many wave-collapse phenomena occurring in classical wave physics. Some of these phenomena are the collapse of Langmuir waves in plasmas [26], and self-focusing of light waves propagating in a medium with a cubic non-linearity [27]. Because of this far-ranging applicability there is an extensive literature devoted to the solution of the non-linear Schrödinger equation under various conditions. Kagan *et al.* have begun to apply some of this accumulated experience to the difficult problem of describing the collapse of a condensate, including both growth and non-linear loss [25].

EXPERIMENT

Magnetic Trap

The apparatus used to produce BEC of ^{7}Li is described most completely in Ref. [20]. A Zeeman slower is used to slow an atomic beam of lithium atoms,

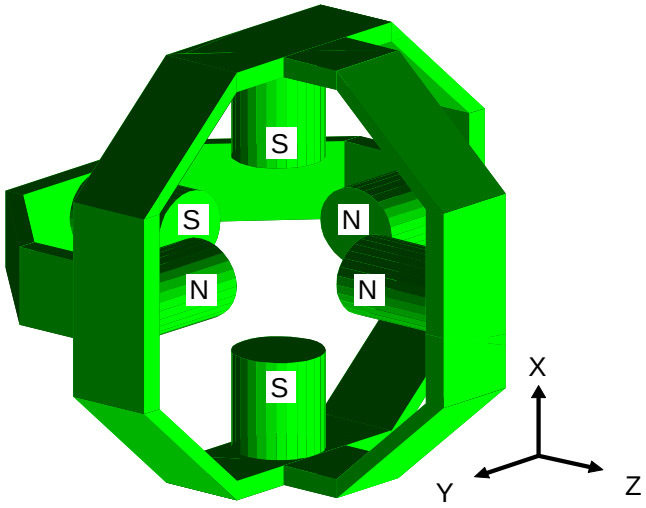

FIGURE 4. Diagram showing the orientation of the cylindrical trap magnets for the permanent magnet trap. The letters indicate the inner tip magnetizations of the NdFeB cylinder magnets. The tip-to-tip magnet spacing is 4.45 cm. The structure around the magnets is a magnetic stainless steel yoke which supports the magnets and provides low reluctance paths for the flux to follow between opposite signed magnets.

which are then directly loaded into a magnetic trap. There is no magneto-optical trap used in the experiment. The magnetic trap is unique in that it is made from permanent magnets, as shown in Fig. 4 [28]. By exploiting the enormous field gradients produced by rare-earth magnets, the resulting trap potential was made nearly spherically-symmetric with a large harmonic oscillation frequency of $\sim$150 Hz. As discussed above, N_m is limited by the tightest trap direction, so the condensate density is maximized for a spherically symmetric potential. In addition, by actively stabilizing the temperature of the magnets the fields are made highly stable, allowing for relatively repeatable and stable experimental conditions. The bias field at the center of the trap is 1004 G.

Evaporative Cooling

After about 1 s of loading, $\sim 2 \times 10^8$ atoms in the doubly spin-polarized $F = 2, m_F = 2$ state are accumulated. These atoms are then laser cooled to near the Doppler cooling limit of 200 μK. At this number and temperature, the phase space density, $n\Lambda^3$, is still more than 10^5 times too low for BEC. The atoms are cooled further by forced evaporative cooling [29]. The hottest atoms are driven to an untrapped ground state by a microwave field tuned just above the $(F = 2, m_F = 2) \leftrightarrow (F = 1, m_F = 1)$ Zeeman transition frequency of approximately 3450 MHz. As the atoms cool, the microwave frequency is reduced. The optimal frequency vs. time trajectory that maximizes the phase-space density of the trapped atoms

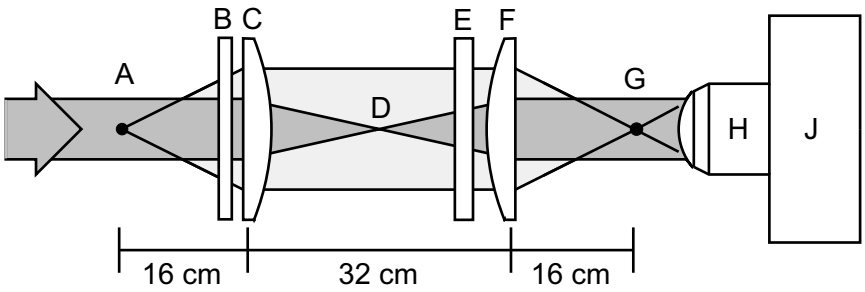

FIGURE 5. A schematic of the imaging system used for *in situ* phase-contrast polarization imaging. A linearly polarized laser beam is directed through the cloud of trapped atoms located at A. The probe beam and scattered light field pass out of a vacuum viewport B, and are relayed to the primary image plane G by an identical pair of 3-cm-diameter, 16-cm-focal-length doublet lenses C and F. The light is then re-imaged and magnified onto a camera J by a microscope objective H. The measured magnification is 19, and the camera pixels are 19 μm square. A linear polarizer E is used to cause the scattered light and probe fields to interfere, producing an image sensitive to the refractive index of the cloud.

is calculated ahead of time [30], and depends on the elastic collision rate and the trap loss rate. The elastic collision rate $n\sigma v$ is roughly 1 s^{-1}, with cross-section $\sigma = 8\pi a^2 \approx 5 \times 10^{-13}$ cm^2. The collision rate is approximately constant during evaporative cooling. We have recently measured the loss rate due to collisions with hot background gas atoms to be $< 10^{-4}$ s^{-1}, and the inelastic dipolar-relaxation collision rate constant to be 1.05×10^{-14} cm^3 s^{-1} [31]. From the low background collision loss rate, we estimate the background gas pressure in the apparatus to be $< 10^{-12}$ torr. Quantum degeneracy is typically reached after 200 seconds, with $N \approx 10^6$ atoms at $T \approx 700$ nK. Lower temperatures are reached by extending the cooling time or by the application of a short, deep cooling pulse.

Phase-Contrast Imaging

After evaporative cooling, the spatial distribution of the atoms is imaged *in situ* using an optical probe. Since the single-particle harmonic oscillator ground state of our trap has a Gaussian density distribution with a $1/e$-radius of only 3 μm, a high-resolution imaging system is required. Because the optical density of the atoms is sufficiently high to cause image distortions when probed by near-resonant absorption [32], we instead use a phase-contrast technique with a relatively large detuning from resonance $\Delta = \pm 250$ MHz. Our implementation of phase-contrast imaging, shown schematically in Fig. 5, is both simple and powerful. It exploits the fact that atoms in a magnetic field are birefringent, so that the light scattered by the atoms is polarized differently from the incident probe light. A linear polarizer decomposes the scattered and probe light onto a common axis, which causes them to interfere. Since the phase of the scattered light is equal to $\alpha/4\Delta$, where α is the

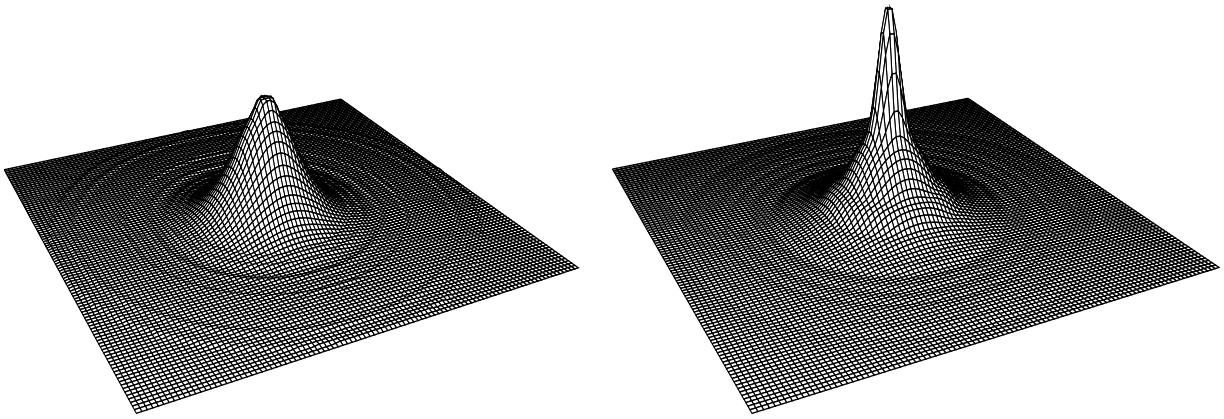

FIGURE 6. Phase-contrast images averaged around the cylindrical axis of the trap. For both cases, $N \approx 23{,}000$ atoms and $T \approx 190$ nK. For the image on the right, $N_0 \approx 1050$, while for the image on the left $N_0 \approx 65$. These images demonstrates our sensitivity to a small number of condensate atoms on a background of a large number of non-condensed atoms.

on-resonance optical density, the spatial image recorded on the CCD camera is a representation of the integrated atomic column density. Phase-contrast polarization imaging is described more fully in Ref. [20].

Fig. 6 shows two images obtained using phase-contrast polarization imaging. For these images, the trap symmetry is exploited by averaging the data around the cylindrical trap axis to improve the signal to noise. The total number of atoms is approximately the same for both images, but on the right T is slightly below T_c and a narrow condensate peak is clearly visible, while for the image on the left, $T \approx T_c$.

Data Analysis

Image profiles are obtained from the averaged data. These profiles are fit with a model energy distribution to determine N, T, and N_0. If the gas is in thermal equilibrium, then any two of N, T, or N_0 completely determine the density of the gas through the Bose-Einstein distribution function. However, if the gas is undergoing the growth/collapse cycles shown in Fig. 3, it certainly is not in thermal equilibrium and a more complicated function is required. Using the quantum Boltzmann equation model, we find that atoms in low-lying levels quickly equilibrate among themselves and the condensate, and that high-energy atoms are well thermalized among each other. Therefore, a three parameter function, including two chemical potentials corresponding to the two parts of the distribution, and a temperature given by the high-energy tail of the distribution, is sufficient to describe the expected non-equilibrium distributions and to determine N_0 [33]. The fits yield an average reduced χ^2 of very nearly 1, indicating that the model is consistent with

the data within the noise level. The procedure was tested by applying it to simulated data generated by the quantum Boltzmann model, and also by comparing the analysis of experimental images of thermalized clouds using both equilibrium and nonequilibrium models. From these tests, the systematic error introduced by the nonequilibrium model is estimated to be not more than ± 50 atoms. The most significant uncertainty in N_0 is the systematic uncertainty introduced by imaging limitations. While the imaging system is nearly diffraction limited, the resolution is not negligible compared to the size of the condensate, and imaging effects must be included in the fit [32]. Imaging resolution is accounted for by measuring the point transfer function of the lens system and convolving this function with the images. Uncertainties in the resolution lead to a systematic uncertainty in N_0 of $\pm 20\%$ [33].

EXPERIMENTAL RESULTS

In this section, we give our experimental results on the observation of limited condensate number [6], and on the collapse of the condensate [33].

Limited Condensate Number

We have measured N_0 for several thousand different degenerate distributions with T ranging between 80 and 400 nK, and for N between 2,000 and 250,000 atoms. In all cases, N_0 is found to be relatively small. The maximum N_0 observed is between 900 and 1400 atoms, depending on the assumed imaging resolution. This measurement is in very good agreement with the mean-field prediction of 1250 atoms.

In the analysis we have assumed that the gas is ideal, but interactions are expected to alter the size and shape of the density distribution. Mean-field theory predicts that interactions will reduce the $1/e$-radius of the condensate from 3 μm for low occupation number to ~ 2 μm as the maximum N_0 is approached [34,7,10,21,22]. If the smaller condensate radius is used in the fit, the maximum N_0 decreases by ~ 100 atoms.

Condensate Collapse

To explore the predicted collapse of the condensate, evaporative cooling is continued well into the degenerate regime, to $N \sim 4 \times 10^5$ atoms at a microwave frequency 100 kHz above the trap bottom. The frequency is then rapidly reduced to ~ 10 kHz and raised again, leaving approximately 4×10^4 atoms. The frequency is swept quickly compared to the collision rate of ~ 3 Hz, so that this "microwave razor" simply eliminates all atoms above a cutoff energy. It thereby creates a definite energy distribution at a specified time whose relaxation to equilibrium can be

followed. Fig. 3 shows the expected trajectory of N_0 in time, for our experimental conditions. For this calculation, we have assumed that N_0 is reduced to zero following a collapse [24].

Although phase-contrast imaging can in principle be nearly nonperturbative, it is not possible to reduce incoherent scattering to a negligible level and simultaneously obtain low enough shot noise to measure N_0 accurately. Each atom therefore scatters several photons during a probe pulse, heating the gas and precluding the possibility of directly observing the evolution of N_0 in time as in Fig. 3. This limitation cannot be overcome by repeating the experiment and varying the delay time τ between the microwave razor and the probe, because the evolution of N_0 is made unrepeatable by random thermal and quantum fluctuations in the condensate growth and collapse processes, as well as experimental fluctuations in the initial conditions. Because of this, however, the values of N_0 occurring at a particular τ are expected to vary as different points in the collapse/fill cycle are sampled. We have observed such variations by measuring N_0 for many similarly prepared samples at several values of τ. Their measured distribution are shown as histograms in Fig. 7. For small τ, N_0 ranges from near zero to about 1200 atoms, as expected if the condensate is alternately filling to near the theoretical maximum and subsequently collapsing. At longer time delays, the histograms change shape, narrowing somewhat at $\tau = 30$ s, and having only small N_0 values at $\tau = 60$ s. The variations in N_0 are uncorrelated with changes in N, T, probe parameters, imaging model parameters, and goodness of fit. To our knowledge, no other explanation for variations of this magnitude has been proposed, so we consider the observation of these variations to strongly support the collapse/fill model.

The histogram data can be compared with the predictions of the quantum Boltzmann model. In the model trajectory shown in Fig. 3, three time domains can be discerned with which the data can be correlated. For $\tau \leq 20$ s, the condensate collapses frequently as the gas is equilibrating. Model histograms for delays of 5 and 10 seconds are similar to each other, and agree qualitatively with the experimentally observed distributions in being broadly spread between 0 and N_m. Around $\tau =$ 20-40 s, equilibrium is reached and N_0 is stabilized for several seconds at a maximum value. As is observed in the data, N_0 declines at later times as atoms are lost through inelastic collisions.

The detailed shape of the model histogram for $\tau \leq 20$ s can be deduced from the dependence of N_0 on time as the condensate fills, since the probability of observing a particular N_0 value is proportional to $(dN_0/dt)^{-1}$ at that N_0 value. After a collapse, the condensate initially fills slowly because the stimulated Bose scattering factor is small. Subsequently, the growth rate increases until N_0 reaches $\sim$100 atoms, when the growth becomes linear. This saturation occurs when the populations of low-lying energy levels in the trap become depleted. Condensate growth is then limited by the rate for collisions between high energy atoms which produce more low energy atoms, which yields a constant fill rate. Because of these effects, a histogram based on our model is significantly peaked at small N_0, and lower but flat between $N_0 = 100$ and N_m.

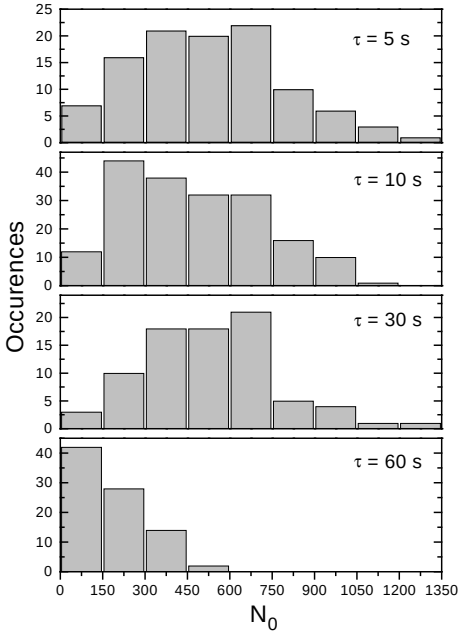

FIGURE 7. Frequency of occurrence of condensate occupation number. For each measurement, a nonequilibrium degenerate gas was produced, allowed to evolve freely for time τ, and then probed. The spread in N_0 values arises as the collapse/fill cycle is sampled at random points.

The observed histograms differ quantitatively from the model predictions in several respects. There is no peak observed at low N_0; rather, a broad peak occurs at $N_0 = 200 - 700$ atoms. A possible explanation for this disagreement is that the condensate does not collapse to zero atoms. If this is the case, then the fact that we do observe some clouds with $N_0 \simeq 50$ atoms indicates that the condensate must collapse to a range of final values. Kagan *et al.* have observed the condensate to collapse to a nonzero value in numerical solutions of the NLSE [25]. However, while those authors found that close to 50% of the condensate was lost during a collapse, our data suggest that considerably smaller remainders are more likely, since a large fraction of our observations show $N_0 < 600$ atoms.

We also observe the frequency of occurrence to drop steadily as N_0 increases, rather than remaining flat up to $N_0 = N_m$ as predicted. This deviation might be explained in either of two ways. If the condensate growth does not saturate but continues to accelerate, then the probability of observing large N_0 values would decrease. This effect might be the result of the decreasing mean-field energy of the condensate with increasing N_0. Alternatively, if the condensate has a larger than expected rate for collapsing at relatively low N_0, then the probability of condensates surviving to large N_0 would decrease. This might be possible if the condensate is typically in a more excited state than expected from the temperature of the gas. Kagan *et al.* predict such excitations to occur during the growth and collapse processes, but quantitative estimates of the effect under our experimental conditions are not yet available. The comparison between theory and experiment at longer

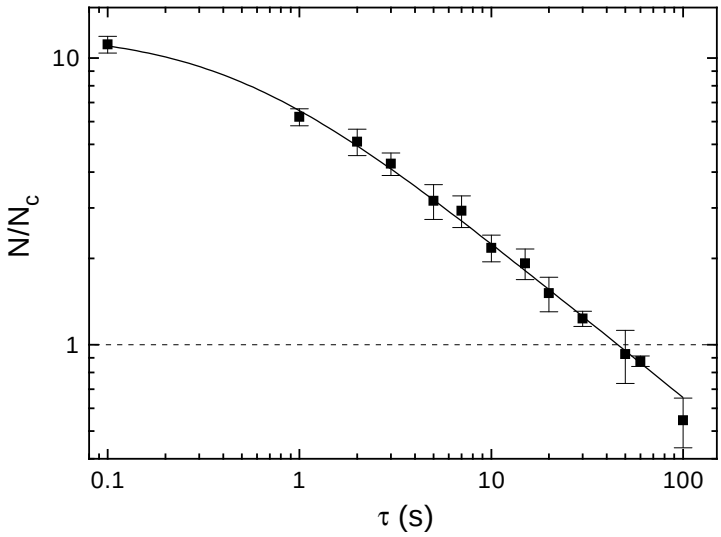

FIGURE 8. Relaxation of degenerate gas to equilibrium. Data were taken as in Fig. 7, but for each image the total number of atoms N and the temperature T were used to determine N/N_c, where $N_c = 1.2(kT/\hbar\omega)^3$. Points represent averages of several measurements, and error bars are standard deviations. The dashed line at $N/N_c = 1$ approximately denotes the point at which equilibrium is reached. The solid curve is a fit to the empirical form $A(1+\kappa\tau)^\gamma$, yielding $A = 12 \pm 1$, $\kappa = 2.1 \pm .7$ s^{-1}, and $\gamma = -.55 \pm .03$.

times is quite good.

The condensate growth and collapse cycle is driven by an excess of noncondensed atoms compared to a thermal distribution. This excess can be examined directly. From N and T, the critical number for the BEC transition, N_c, is calculated and the ratio N/N_c plotted as a function of delay time in Fig. 8. The ratio decays according to a power law, which signifies that a nonlinear process governs equilibration. This nonlinearity is reasonable since the rate of decay of the excess atoms should depend both on the excess number and on the collision rate, which in turn depends on N and T. Since $N_0 \ll N$, equilibrium is reached when $N/N_c \approx 1$, which occurs at $\tau \approx 40$ seconds. This time is consistent with the delay required to accurately fit the image data with an equilibrium model, and with the results of the quantum Boltzmann model. Comparison of Figs. 7 and 8 shows that the equilibration time is also consistent with the changing shape of the measured histograms. This further strengthens the conclusion that the variations in N_0 are related to the growth and collapse of the condensate during the equilibration process, since the distribution of N_0 values changes when the population imbalance driving condensate growth is eliminated.

CONCLUSIONS

These observations provide quantitative support for the applicability of mean-field theory to attractive gases. The measurements described here are the first indicator of the complex dynamics accompanying BEC in a gas with attractive interactions. We believe that they support the collective collapse/fill model as a useful framework for considering such systems. It is clear, however, that additional theoretical work is necessary to accurately describe the collapse in detail. Experimentally, we are pursuing more direct methods of observing the growth and collapse of the condensate, including minimally perturbative measurement techniques and controlled triggering of a collapse using an optically induced Feshbach resonance [35]. By such means, we hope to further our understanding of this novel and interesting state of matter.

REFERENCES

1. M. H. Anderson, J. R. Ensher, M. R. Matthews, C. E. Wieman, and E. A. Cornell, Science **269**, 198 (1995).
2. C. C. Bradley, C. A. Sackett, J. J. Tollett, and R. G. Hulet, Phys. Rev. Lett. **75**, 1687 (1995).
3. K. B. Davis, M.-O. Mewes, M. R. Andrews, N. J. van Druten, D. S. Durfee, D. M. Kurn, and W. Ketterle, Phys. Rev. Lett. **75**, 3969 (1995).
4. N. Bogolubov, J. of Phys. **XI**, 23 (1947).
5. H. T. C. Stoof, Phys. Rev. A **49**, 3824 (1994).
6. C. C. Bradley, C. A. Sackett, and R. G. Hulet, Phys. Rev. Lett. **78**, 985 (1997).
7. R. J. Dodd, M. Edwards, C. J. Williams, C. W. Clark, M. J. Holland, P. A. Ruprecht, and K. Burnett, Phys. Rev. A **54**, 661 (1996).
8. Y. Kagan, G. V. Shlyapnikov, and J. T. M. Walraven, Phys. Rev. Lett. **76**, 2670 (1996).
9. E. Shuryak, Phys. Rev. A **54**, 3151 (1996).
10. H. T. C. Stoof, J. Stat. Phys. **87**, 1353 (1997).
11. M. Ueda and A. J. Leggett, Phys. Rev. Lett. **80**, 1576 (1998).
12. K. Huang, *Statistical Mechanics*, 2 ed. (John Wiley & Sons, New York, 1987).
13. J. Weiner, V. S. Bagnato, S. Zilio, and P. S. Julienne, review to be published.
14. E. R. I. Abraham, W. I. McAlexander, C. A. Sackett, and R. G. Hulet, Phys. Rev. Lett. **74**, 1315 (1995).
15. E. R. I. Abraham, W. I. McAlexander, J. M. Gerton, R. G. Hulet, R. Côté, and A. Dalgarno, Phys. Rev. A **55**, R3299 (1997).
16. C. C. Tsai, R. S. Freeland, J. M. Vogels, H. M. J. M. Boesten, B. J. Verhaar, and D. J. Heinzen, Phys. Rev. Lett **79**, 1245 (1997).
17. F. Dalfovo, S. Giorgini, L. P. Petaevskii, and S. Stringari, review to be published.
18. E. M. Lifshitz and L. P. Pitaevskii, *Statistical Physics, Part 2* (Butterworth-Heineman, Oxford, 1980).

19. P. A. Ruprecht, M. J. Holland, K. Burnett, and M. Edwards, Phys. Rev. A **51**, 4704 (1995).
20. C. A. Sackett, C. C. Bradley, M. Welling, and R. G. Hulet, Appl. Phys. B **65**, 433 (1997).
21. M. Houbiers and H. T. C. Stoof, Phys. Rev. A **54**, 5055 (1996).
22. T. Bergeman, Phys. Rev. A **55**, 3658 (1997).
23. K. Singh and D. Rokhsar, Phys. Rev. Lett. **77**, 1667 (1996).
24. C. A. Sackett, H. T. C. Stoof, and R. G. Hulet, Phys. Rev. Lett. **80**, 2031 (1998).
25. Y. Kagan, A. Muryshev, and G. Shlyapnikov, Phys. Rev. Lett **81**, 933 (1998).
26. V. E. Zakharov, Sov. Phys. JETP **35**, 908 (1972).
27. V. E. Zakharov, Sov. Phys. JETP **41**, 465 (1976).
28. J. J. Tollett, C. C. Bradley, C. A. Sackett, and R. G. Hulet, Phys. Rev. A **51**, R22 (1995).
29. W. Ketterle and N. J. van Druten, in *Advances in Atomic, Molecular, and Optical Physics* (Academic Press, San Diego, 1996), No. 37, p. 181.
30. C. A. Sackett, C. C. Bradley, and R. G. Hulet, Phys. Rev. A **55**, 3797 (1997).
31. J. M. Gerton, C. A. Sackett, B. J. Frew, and R. G. Hulet, to be published.
32. C. C. Bradley, C. A. Sackett, and R. G. Hulet, Phys. Rev. A **55**, 3951 (1997).
33. C. A. Sackett, J. M. Gerton, M. Welling, and R. G. Hulet, to be published.
34. F. Dalfovo and S. Stringari, Phys. Rev. A **53**, 2477 (1996).
35. P. O. Fedichev, Y. Kagan, G. V. Shlyapnikov, and J. T. M. Walraven, Phys. Rev. Lett. **77**, 2913 (1996).